Biomedical Physics & Engineering Express

ENDORSED BY IPEM Institute of Physics and Engineering in Medicine

ACCEPTED MANUSCRIPT

Biocompatibility and bioactivity of hardystonite-based nanocomposite scaffold for tissue engineering applications

To cite this article before publication: Mozhdeh Hamvar *et al* 2020 *Biomed. Phys. Eng. Express* in press https://doi.org/10.1088/2057-1976/ab7284

Biocompatibility and bioactivity of hardystonite-based nanocomposite scaffold for tissue engineering applications

Mozhdeh Hamvar[1], Hamid Reza Bakhsheshi-Rad[1,2,*], Mahdi Omidi[1], Ahmad Fauzi Ismail[2], Madzlan Aziz[2], Filippo Berto[3], Xiongbiao Chen[4]

[1]Advanced Materials Research Center, Department of Materials Engineering, Najafabad Branch, Islamic Azad University, Najafabad, Iran
[2]Advanced Membrane Technology Research Center (AMTEC), Universiti Teknologi Malaysia, 81310 Skudai, Johor Bahru, Johor, Malaysia
[3]Department of Mechanical and Industrial Engineering, Norwegian University of Science and Technology, 7491 Trondheim, Norway
[4]Department of Mechanical Engineering, College of Engineering, University of Saskatchewan, Saskatoon, SK S7N 5A9, Canada

Corresponding author: H.R. Bakhsheshi-Rad (rezabakhsheshi@gmail.com; rezabakhsheshi@pmt.iaun.ac.ir)

Abstract

Bone injury, especially bone damages due to the removal of bone tumors, is one of the most important issues in the field of therapeutic research in tissue engineering applications. In this context, ceramic-based composites have attracted widespread attention since they have mechanical properties close to the natural bone, hence providing similar conditions for the extracellular matrix (ECM). Thus, in this study, hardystonite and diopside (HT-Di) scaffolds containing various diopside amounts from 5 to 25 wt.% were prepared by the space holder method. The results revealed that the fabricated scaffolds contain 70-75% porosity with a pore size of 300-500 μm and a compressive strength of about 0.54 to 1.71 MPa which is perfectly in the range of the compressive strength of the sponge bone. Noticeably, great apatite formation ability was observed in the scaffold with diopside, although the scaffold without diopside showed poor bioactivity. The MTT assay depicted that the inclusion of diopside into hardystonite scaffold resulted in dramatic enhancement in the MG-63 cell viability. Moreover, the scaffold with diopside offered greater cell attachment and spreading than the scaffold without diopside. Therefore, the synergistic effects of the scaffold with 12.5 wt.% of diopside, including great mechanical characteristic, excellent bioactivity, and appealing biocompatibility enable it to be an appealing choice for bone tissue engineering applications.

Keywords: Nanocomposite scaffolds; Hardystonite; Bioactivity; Bone tissue engineering

1. Introduction

In recent years, despite many advances in bone tissue restoration, the present methods such as bone grafts have many limitations [1]. Besides, in spite of the fact that material science has significantly contributed to the development of bone substitutes, treatments of many severe bone lesions are associated with serious issues, and no obvious repairs are practically presented [1, 2]. Moreover, the use of these methods is associated with problems such as undesirable immune response, unwanted structural changes in the body tissue, and requirement for multiple surgical operations [3, 4]. That is why bone tissue engineering has been considered as an emerging and progressive field in recent years [5]. In this relation, in order to maintain tissue function and its regeneration via using tissue engineering, a pattern or scaffold is required to act as a temporary field for the growth of cells and to cause the formation and growth of bone tissues [6, 7].

In bone tissue repair, it is essential to use biomaterials with proper characteristics of a scaffold [8]. Recently, composite scaffolds have been used to achieve more desirable properties [3]. In this study, due to its favorable properties, the hardystonite-diopside nanocomposite was used as a bioactive ceramic to design bone scaffolds. Recently, researchers have found that in order to achieve successful bone substitutes with long sustainability, a biodegradable, bioactive, and biocompatible matrix with suitable mechanical properties is required [5, 9-12]. To achieve this aim, a wide range of natural and synthetic materials have been employed as scaffolds and/or bone composites. Over the past few decades, the use of calcium silicate bioceramics with SiO_2-CaO-Na_2O-P_2O_5 compounds, which have desirable properties such as biocompatibility, non-toxicity, and stability in the physiological environment of the body, has led to a dramatic evolution in biomedical applications [9, 13-15]. These materials have been widely employed to repair or replace damaged tissues, such as the hip, knee, shoulder, and other orthopedic applications, and also to replace damaged heart valves or dental implants [11, 16]. In contrast to hydroxyapatite [17, 18] and various other ceramic scaffolds, the Mg-containing bioceramics have demonstrated higher benefit for bone tissue regeneration. Among these bioceramics, hardestonite ($Ca_2ZnSi_2O_7$) has presented suitable degradation rate and higher potential for apatite formation and tissue regeneration [19, 20].

Ramaswamy et al. [21] examined the biological characteristics of bone cells in calcium-silica based ceramics. Their results indicated that hardestonite had the highest adhesion levels and no toxicity was observed. Zreiquat et al. [2] investigated the effect of adding strontium and zinc to

the calcium-silicone ceramics for tissue engineering applications. They reported that hardystonite implants in the damaged femur of a rabbit had a higher recovery rate and a higher osteogenic growth rate compared with beta-tricalcium phosphate. They also reported that these scaffolds were non-toxic and significantly improved the viability of osteogenic cells.

A widely recognized method to enhance the mechanical performance of hardestonite scaffold is the synthesis of hardestonite matrix composite scaffolds. In numerous applications, there is certainly a demand for a composite material with a number of certain characteristics. Composite-based materials are composed of two or even more basic components with the desired characteristics of each of them and the simultaneous reduction of the restriction of every single component [22]. In this regard, it was reported [23-27] that nanostructured materials presented higher strength, toughness, hardness, ductility, elastic modules, and specific surface area compared with other materials. Taking into account the properties of hardestonite and diopside, the mixture of these types of bioceramics is actually productive for obtaining nanocomposite materials with appropriate mechanical and bioactivity properties [28, 29]. Diopside ($CaMgSi_2O_6$) belongs to the silicate-based ceramic families and is employed for synthetic bone and dental root due to its excellent apatite formation capability and greater mechanical strength including bending strength and fracture toughness compared to HA [30, 31]. Iwata et al. [32] evaluated the apatite formation ability of diopsides synthesized via co-precipitation (CPT) method and their results showed that owing to the dissolution of calcium and silicon ions, the apatite layer was well formed on the surface of diopside in the simulated body fluid (SBF). In this context, it was reported [11] that the apatite layer was easily formed on the surface of porous glass ceramics containing diopside. Likewise, Wu et al. [33] assessed the cell attachment capability of hardystonite and their results demonstrated that hardystonite presented a very high potential for adhesion of the bone cells to its surface. Wang et al. [34] also demonstrated that the porous hardystonite presented appropriate degradation rate for biological applications. Xiong et al [35] examined the dissolution rate of $CaSiO_3$ bioceramics containing calcium and silicon ions and their results revealed that the porous layers containing zinc reduced the dissolution rate and had no destructive effect on cell adhesion of the osteogenic cells and formation of apatite on the scaffold surface.

A variety of fabrication methods (including the space holder method) are actually employed for producing porous scaffolds [36]. This approach is widely recognized because the porosity and

pore size of scaffolds could be effortlessly manipulated by employing various spacers including carbamide particles, sodium chloride [2] and magnesium particles performing like porogens inside the scaffolds. Therefore, fabrication of hardystonite-diopside nanocomposite scaffolds with great mechanical properties and biocompatibility has attracted considerable attention for tissue engineering applications. In this study, hardystonite-diopside nanocomposite scaffolds containing various amounts of diopside were fabricated via the space holder method and were subsequently examined in vitro to assess their potential to be used in tissue engineering applications.

2. Experimental procedure

Hardystonite and diopside powders were prepared via the sol–gel method from tetraethyl orthosilicate, ($(C_2H_5O)_4Si$, TEOS), magnesium nitrate hexahydrate ($Mg(NO_3)_2{\cdot}6H_2O$), and calcium nitrate tetrahydrate ($Ca(NO_3)_2{\cdot}4H_2O$), zinc nitrate hexahydrate ($Zn(NO_3)_2{\cdot}6H_2O$) as raw materials and HNO_3 as a precipitant. For diopside fabrication, $Mg(NO_3)_2{\cdot}6H_2O$ was employed instead of $Zn(NO_3)_2{\cdot}6H_2O$. Finally, to obtain the nanostructure powder, each powder was milled in a planetary ball mill (Retsch PM400) for 10 h with the ball-powder weight ratio of 10/1, the rotational speed of 300 rpm, and the powder mass of 10 gr. The space holder method was utilized to fabricate the scaffolds. Briefly, the HT powder was mixed with different Di powder contents (0, 5, 12.5 and 25 wt.%). The space holder method was subsequently applied to create Mon scaffolds, mixing NaCl (as the spacer; particle size 300–500 μm) and HT-Di nanopowder at a weight ratio of 75:25. The powder was eventually pressed under 110 MPa into a cylindrical form (10 mm diameter × 15 mm height) and then sintered at 1300 °C for 4 h at a heating rate of 5 °C/min. This procedure was followed by removing the NaCl particles by immersing the specimens in distilled water for 24 h. Fig. 1 presents the fabrication procedure of hardystonite-diopside scaffolds.

The interconnected and true porosity were calculated using the Archimedes principle. The total porosity of the scaffolds consisted of interconnected and closed pores according to the following equation:

$$\text{Total porosity} = 1 - \frac{Wd}{\rho\,(Wd-Ws)} \times 100 \qquad (1)$$

where Wd, Ws, and ρ are the weight of the scaffold in air, the weight of the sample suspended in water, and the true density of the composite as follow:

$$\rho\text{composite} = (\text{wt.}\% \times \rho\text{Di}) + (\text{wt.}\% \times \rho\text{HT}) \quad (2)$$

In order to study the compressive strength, the samples were prepared with the dimensions of an approximate diameter of 6 mm and a height of 10 mm. The compression test was performed uniaxially using a Zwick/Roell Z050 machine under a load of 25 KN. In this test, the force was applied at a speed of 0.5 mm/min until it reached a strain of over 10%.

For cellular assay, in order to sterilize the scaffolds, their surfaces were first coated by alcohol and then placed under ultraviolet rays for 30 min. In the next step, the scaffolds were immersed in a phosphate buffered saline (PBS) solution containing 1% antibiotic and subjected to UV rays for 30 min. Eventually, the PBS was removed and the scaffolds were placed in a 24-part container under sterilized conditions. In this study, for performing all the cellular tests, three groups of scaffolds were used as repetitions. Moreover, to culture the human osteosarcoma cell lines MG-63 (NCBI C-555, National Cell Bank of Iran, Pasteur Institute), DMEM medium containing 15% fetal bovine serum (FBS) and 100 g/ml Penicillin-Streptomycin were used. Cell suspensions with a number of 15×10^3 were cultured in a polystyrene culture container containing the scaffold samples for 24 h under the conditions of 95% air and 5% carbon dioxide. The samples were then fixed by 4% formaldehyde. Then in the dark condition, the fluorescent solution was added for 10 min so that the nucleus of the cells turned blue. In the next step, the morphology of the stained and cultured cells was observed on the specimens using an Olympus fluorescence microscope [20]. The in vitro cytotoxicity of HT-Di scaffolds was determined by indirect 3-(4,5-dimethylthiazol -2-yl)-2,5-diphenyltetra-zolium-bromide (MTT, Sigma, Saint Louis, USA) assay according to Ref [31]. Nuclear staining with DAPI (4′,6-diamidino-2-phenylindole, blue fluorescence in live cells) was performed to examine MG-63 cell proliferation on the HT-Di scaffolds under fluorescence microscopy. In order to determine the amount of calcium precipitated by bone cells, Alizarin red staining was used for 7 days. For this purpose, after the culture of MG-63 cells in the vicinity of the samples, the outer environment of the cells was removed for 7 days and the cells were fixed by 4% formaldehyde. After that, the prepared 1% Alizarin red color was added in a Tris buffer with a pH value of about 8 for 15 min according to Ref. [22].

To study the bioactivity behavior, each of the HT-Di scaffolds was soaked in 100 mL of SBF at 36.5 ± 1 °C for 28 d with a chemical composition as listed in Table 1 [37]. After this period, the scaffolds were removed from the SBF cups and rinsed with distilled water and dried in the open air. Since the conditions of scaffold placement in the solution depend on the area of the samples and the volume of the solution and also affect the formation of the apatite layer, the area of the cylindrical shapes was calculated first, and then according to equation (3), the volume of the solution consumed was calculated.

$$Vs = \frac{\mathrm{Sa}}{10} \quad (3)$$

where V_s is the volume of solution in mL and S_a is the surface area of the samples. Changes in the pH of SBF solution, following exposure to scaffolds, as a function of time, were also examined. For measurement of the degradation rate, the scaffold was soaked in the PBS solution for various durations from 7 to 28 days and the result was presented as the weight loss as a function of the immersion time according to Ref. [38].

Microstructures of the HT-Di scaffolds were studied using transmission electron microscopy (TEM, Hitachi HT7700, Japan) and scanning electron microscopy (SEM, JEOL JSM-6380LA, Japan) equipped with energy dispersive X-ray spectroscopy (EDS; JEOL Inc., Tokyo, Japan). To illustrate the surface functional groups of the specimens, Fourier transform infrared (FTIR) spectroscopy (Bruker; Germany) in a wave number ranging from 4000 to 400 cm^{-1} was employed. It is also worth noting that the porosity diameter in the samples was calculated using the ImageJ software. An X-ray diffractometer (Siemens D5000) was used to determine the phase components using Cu-Kα radiation (45 kV, 40 mA) over the diffraction angles (2θ) of 20–80° at a scanning speed of 4°/min. Finally, the crystallite size was determined by the Williamson–Hall method [39] according to the following equation:

$$\frac{\beta}{2}\mathrm{Cot}\,\theta = \frac{0.45\,\lambda}{\mathrm{Sin}\theta.D} + \varepsilon \quad (4)$$

where β accounts for the diffraction peak width at the mid-height, λ indicates X-ray wavelength, and D is the average crystallite size (nm). The microstrain and Bragg diffraction angle are indicated in the formula by ε and θ, respectively.

3. Results and discussion

3.1. Characterization of the powders and scaffolds

The X-ray diffraction patterns of hardystonite samples and the diopside-reinforced hardystonite sample after sintering at 1300 °C are shown in Fig. 2a. According to this figure, the absence of impurities such as willemite at this temperature can be attributed to the homogenization of compounds and the activation of their surface by mechanical alloying. According to the patterns, hardystonite (JCPDS 01-075-0916) and diopside (JCPDS 01-071-1067) nano-powders were fabricated without any secondary phases. In this method, the bonding and continuous breakdown of ceramic materials lead to a reduction in the crystallite size of the synthesized powders. The average crystallite size of hardystonite and diopside synthesized powders was estimated to be 82 and 87 nm by the Williamson-Hall method (Eq. 3), respectively.

The FTIR spectrum (Fig. 2b) of the HT scaffold containing various Di amounts prior to soaking in SBF presented the typical absorption bands that are attributed to Si-O-Si in the range of 1040, 966, 912, 681, and 621 cm^{-1} [40,41]. The Zn-O band was found at around 521 cm^{-1} while the typical absorption peak of Ca-O and Mg-O was observed at 511 cm^{-1} and 471 cm^{-1} which verified the existence of Di within the HT-based scaffolds [40,41]. It is worth mentioning that there is a good agreement between the XRD results and FTIR spectrometry data.

Fig. 2

The TEM images of the hardystonite-diopside synthesized powders are shown in Fig. 3. As can be seen, the synthesized HT powders have a particulate morphology with an average size of 87± 3 nm. Similarly, the particles of diopside powder possess an irregular morphology with the average size of 80 ± 3 nm. In contrast to the HT and Di nanopowder, the composite consists of a number of particles which agglomerated together as a result of the high surface energy of each individual particle [38]. The nanostructure of these powders indicated the high reactivity due to the high surface area (high surface to volume ratio) of these powders. In this view, it was suggested [42] that nano-bioceramics presented higher mechanical properties than their micro-grain counterparts.

Fig. 3

SEM images and pore size histogram of HT and HT-Di scaffolds containing various amounts of HT are shown in Fig. 4. The image exhibits the formation of porous scaffolds comprising of interconnected pores with a typical size in the range of 300-500 μm. The pores in the range of

50-300 μm are able to provide an appropriate environment for bone tissue ingrowth and exchange of body fluid [5, 38]. According to the distribution histograms, escalating the diopside phases leads to slight diminished pore size. As can be noticed, the size of pores decreased with escalating the diopside content which might be attributed to the increased sinterability of the scaffolds. The sintering temperature of the specimens was chosen close to the melting point of diopside at around 1390 °C. For this reason, diopside nano-powder may work as a sintering aid to enhance the mechanical properties of the scaffolds [41-44]. Also, the EDX spectra of HT-12.5Di showed the existence of Mg, Si, Zn, Ca and O which further verified the presence of diopside in the matrix of hardystonite and the absence of NaCl after sintering, since the typical peaks of Na and Cl were not found.

Fig. 4

3.2. Mechanical properties evaluation

The compressive strength stress-strain of hardystonite-diopside scaffolds is shown in Fig. 5. According to this figure, in all scaffolds, three distinct regions can be observed. According to previous studies by Qomi et al. [45] about the porous diopside scaffolds synthesized using the space holder method, these areas are defined as follows. The first region is a linear region in which stress has an almost direct relationship with strain, and this region continues up to the ultimate compressive strength. The second region indicates the failure of the pores under pressure, in which the pores collapse. In the third zone, the scaffold compression and the pore closure occur during the pressure increase. The compressive stresses of the samples increase with increasing the diopside content. It can also be observed that the ultimate compressive strength for the HT, HT-5Di, HT-12.5Di, and HT-25Di samples was about 0.54, 0.97, 1.71 and 1.51 MPa, respectively which were completely in the range of the compressive strength of the sponge bone (0.2 to 4 MPa), implying the high capability of the fabricated scaffolds for application in bone tissue engineering. By adding the diopside to the hardystonite scaffold up to 12.5 wt.%, the compressive strength improved. In fact, diopside acts as a filler and flux in the composite, hence resulting in a reduction in the curing temperature and subsequently improving mechanical properties. The surface under the stress-strain curve in hardystonite-dioptside scaffolds is higher compared to the hardystonite scaffold, indicating the higher toughness of the hardystonite-dioptside scaffold. However, further diopside addition reduces the compressive strength due to

the agglomeration of the diopside phase within the grain boundaries which work as a crack location and thus reduce the compressive strength.

Furthermore, the existence of diopside in the hardystonite matrix can concurrently enhance the sintering trend and reduce the grain growth. Similar findings had been noted in other studies concerning the existence of diopside in the matrix of Al_2O_3 which resulted in reduction of the grain growth of alumina and an enhancement in the compactness rate [46]. It is apparent that the condensed samples of synthesized nanocomposite powder sintered at an elevated temperature (1300 °C) display substantial enhancements in mechanical properties in comparison with single phase hardystonite and diopside which in turn makes it an appropriate candidate for employing in tissue engineering applications.

Fig. 5

3.3. In vitro bioactivity

Scaffolds with good bioactivity can easily establish a chemical bond with the surrounding tissues. It is worth considering that scaffolds for bone substitution require suitable bioactivity which is commonly identified by the capability to promote the formation of apatite layer on the scaffold surface after soaking in the SBF solution. The formation of apatite layer on the porous scaffold surface might offer an appropriate substrate for attachment and proliferation. Therefore, a solid bond with the adjacent tissue might be generated that will support the biological fixation of the porous scaffold within the bone defect [41]. In order to investigate the apatite formation capability of hardystonite-diopside composites, the samples were immersed in the SBF solution for 28 days [24]. Fig. 6 exhibits the SEM images of the apatite layer formed on the scaffolds along with the EDS analysis. As can be observed, SEM images (low magnification) of HT and HT-Di (x = 5, 12.5, and 25 wt.%) scaffolds verify the formation of a compacted apatite film on the entire surface of scaffolds. Based on the image, the formation of apatite on the scaffold surface resulted in the reduction of the pore size and interconnectivity. Furthermore, the amount of the micro-pores presence inside the pore wall decreased after the deposition of the apatite layer on the scaffold surface. However, high magnification images exhibit that the surface of scaffolds consists of spherical aggregates of apatite which are generally about 0.8-1.4 μm in diameter. For all the HT-Di scaffolds, the apatite morphology is comparable and does not change with increasing the Di amounts. However, a slight reduction in particle size is observed. These results with regard to the formation of apatite on the surface of the scaffolds suggest that the

inclusion of various amounts of Di as the reinforcement phase could substantially improve bioactivity and mechanical properties of the hardystonite matrix. In this relation, it was suggested that the presence of the calcium ions in diopside could exchange with the H^+ existence in the medium and generate a hydrated silica film which in turn can present suitable sites for PO_4^{3-} nucleation on the scaffolds [38]. These sites stimulate the formation of apatite film on the scaffold surface in the physiological medium. The EDS mapping (Fig. 7) of the whole scaffolds verifies that Ca and P are well distributed on the surface of scaffolds which further confirms the deposition of hydroxyapatite on scaffolds surface. The Ca/P atomic ratio elevated from 1.39 to 1.49 with escalating diopside from 5 to 25 wt.% within the hardystonite matrix which is in good agreement with the mapping results.

Fig. 6

Fig. 7

Fig. 8 exhibits the schematic description of the apatite formation process for the HT-Di scaffold in the SBF solution. When the scaffolds are exposed to the SBF, the dissolution of the hardystonite-diopside scaffolds occurs, resulting in the exchange and release of Ca^{2+} with H_3O^+ or H^+ in the solution [47]. After the dissolution of hardystonite, the reduction of SiO_2 in the solution causes some changes in the Si-O-Si bonds and the formation of Si-OH silane groups as demonstrated by equation (5):

$$Si - O - Si + H_2O \rightarrow Si - OH + HO - Si \quad (5)$$

In this case, the addition of Si-OH groups leads to the formation of a SiO_2 hydrated gel, which ultimately consumes the alkaline cations. On the other hand, the SiO_2 hydrated gel film is negative and it can react with the calcium and phosphate ions in the SBF [47]. Meanwhile, the Mg^{2+} and Ca^{2+} ions and OH^- ions dissolve in the surface and continuously increase to reach the solubility level of apatite in the SBF in accordance with reaction (6):

$$10Ca^{2+} + 6PO_4^{3-} + 2OH^- \rightarrow Ca_{10}(PO_4)_6(OH)_2 \quad (6)$$

The above mentioned factors increase the apatite nucleation and the probable growth of the apatite layer on the hardystonite-diopside scaffold. The samples were immersed in the SBF solution (pH = 7.40) at 37 °C for 14 days to examine the pH variations. Fig. 9a shows the pH variation graph of HT-Di scaffolds for a period of 28 days. As can be observed, the lowest pH change rate is associated with the neat hardestonite scaffold. As it was previously mentioned, these results can be due to the very low degradation rate and the highest chemical stability of hardystonite compared to other calcium silicate compounds [48, 49]. By adding diopside, it is

observed that these changes in the pH value have increased significantly. The reason for this trend can be the increase in the rate of degradation of hardystonite by adding diopside, since according to the previous studies, diopside has a lower chemical stability compared to hardystonite. Therefore, addition of diopside to hardystonite accelerates the hardystonite degradation process. Consequently, the escalation of calcium and magnesium ions release and their exchange with H^+ or H_3O^+ from SBF can be taken into account as the main cause of alkalinity and escalation of the pH value.

The mass loss (Fig. 9b) of HT scaffold containing various amounts of Di after soaking in PBS for 28 days indicates that the mass loss of scaffolds elevated with lengthening the incubation time and increasing the diopside amount. It might be attributed to the smaller grained structure and greater interface generated between the scaffold and the solution that enhance the degradation rate of the HT-base scaffolds. In this context, it was suggested that the capability of apatite deposition was strongly attributed to the degradability of the composite. Thus, by increasing the diopside amount, capability of apatite deposition and degradability of the HT-base scaffolds were also elevated.

The FTIR spectrum of the HT scaffold containing various Di amounts after soaking in SBF indicated that the typical absorption peaks of PO_4^{3-} groups were observed at 1013, 971, 916, 624 and 509 cm^{-1} while the absorption band attributed to Si-O was detected at 839 cm^{-1}. Moreover, the absorption peak of OH groups in the structure of apatite was detected at 1632 cm^{-1} [40, 41]. The typical peaks at 3432 cm^{-1} were assigned to the O-H bands in H_2O. Hence, it could be concluded that apatite nucleation and formation had taken place after soaking in SBF. The absorption peak of the carbonate groups was found at 1424 cm^{-1} which further verified the formation of HA on the scaffold surface. The result of FTIR spectrometry is in good agreement with the EDS results.

Fig. 8
Fig. 9

3.4. Cell culture

The DAPI staining of MG-63 cells nuclei on the HT-Di with different diopside contents in Fig. 10a-d depicts that the cells are attached strongly and spread on the scaffolds containing diopside, while the scaffolds without diopside show poor cell attachment. Fluorescent images also proved that the cell attachment on the scaffolds is diopside concentration dependent and more cells were grown and proliferated on the scaffold containing 25 wt.% of diopside. This shows that the

addition of diopside to the hardystonite scaffold allows the cells to penetrate into the scaffold and migrate in a manner similar to the extracellular field. Increasing sensitive external receptors will exacerbate the proliferation of osteoblasts and chemotherapy. Similarly, the presence of magnesium and calcium ions in diopside can increase the proliferation of the osteoblast cells because magnesium ions may be attached to the receptors and extracellular changes in magnesium ions may cause cellular connections. The result of another study revealed that the presence of some ions, such as silicon, calcium, and magnesium, resulted from dissolution of Si-based ceramics containing Mg could increase cell proliferation [11]. In addition, previous studies [9] have shown that silicon plays a major role in the development of skeletal system. The presence of the silicon element in the hardystonite and diopside scaffold can support the proliferation and growth of osteogenic cells that are useful for bone formation. Given these reasons, the formation of an enriched silicon layer on the surface of the hardystonite-diopside scaffold can accelerate cell proliferation.

Fig. 10e reveals the results of MTT assay carried out on the scaffolds with various diopside amounts after different incubation times. The findings display that the cell viability in the scaffolds with diopside is considerably greater in comparison with the HT scaffold without diopside. As can be noticed, cell viability in all scaffolds is over 75% after 5 days, implying the biocompatibility of the scaffolds. Having said that, it is essential to consider that the addition of diopside to the hardystonite matrix has drastically enhanced its biological properties, to the effect that the scaffold with 25 wt.% diopside on the fifth day revealed a viability of about 96% that is close to the control . The scaffold containing more diopside offered appropriate physiological environment for cell attachment which further confirmed its biocompatibility. Actually, the release of the calcium ion from the dissolved diopside has a substantial effect on the cellular and metabolic activities of the MG-63 cells. This finding demonstrates that the whole scaffolds containing diopside encountered dissolution during the cell culture procedure. It is apparent that the concentrations of Ca and Mg ions are elevated with escalating the diopside content in the scaffolds.

Fig. 10

Alizarin red (AR) staining was performed to illustrate the effect of the HT-Di scaffolds on Ca-P of MG-63 cells (Fig. 11). Alizarin red is a color used to indicate the mineralization or the capability to produce calcium by the cell. As can be seen, red veins in the yellow field represent

the calcium secretion and deposition by bone cells. The important point is that calcium deposition has significantly increased with increasing the diopside amount in the synthesized composites. Overall, in this study, it was shown that escalating the diopside amount amplified the apatite formation of the scaffolds. Therefore, according to the previous statement, the high ability of apatite formation and bioactivity of diopside and the ability to express ostegenic genes by diopside can be a good justification for improving alkaline phosphatase activity and the ability to release calcium by increasing diopside.

Fig. 11

4. Conclusion

In this study, hardystonite-based scaffolds with different diopside contents were successfully prepared via the space holder method and subsequently the effect of increasing the Di content on mechanical and cellular behavior of the as prepared HT-xDi scaffolds was investigated. The synthesized scaffolds have a porous structure with an average porosity diameter of about 300-500 μm and a porosity of 70-75% for application in bone tissue engineering. Incorporation of diopside up to 12.5 wt.% into the hardystonite matrix resulted in the enhancement of the compressive strength while further addition (25 wt.%) reduced the compressive strength. The bioactivity finding depicted the nucleation of hydroxyapatite in the surface of all scaffolds and more apatite deposition was found on the scaffold with higher diopside content after soaking in SBF. The MTT assay revealed that the cell viability of the scaffold with diopside was drastically enhanced. The HT scaffold with diopside experienced more cell attachment and spreading than the scaffold without diopside. Taken together, the addition of diopside to the HT scaffold causes the escalation of mechanical and biological properties and, as a consequence, would be beneficial for potential use of these scaffolds in bone tissue engineering applications.

Acknowledgements

The authors thank the Malaysian Ministry of Higher Education (MOHE) and Universiti Teknologi Malaysia (UTM), Saskatchewan Health Research Foundation (SHRF) and Natural Sciences and Engineering Research for providing the facilities for this research.

Conflict of interest

The authors declare that they have no conflict of interest.

References

[1] M.N. Rahaman, D.E. Day, B. Sonny Bal, Q. Fu, S.B. Jung, L.F. Bonewald, and A.P. Tomsia, Bioactive glass in tissue engineering. Acta Biomater., 2011. 7: 2355-2373.

[2] H. Zreiqat, Y. Ramaswamy, C. Wu, A. Paschalidis, Z. Lu, B. James, O. Birke, M. McDonald, D. Little, and C.R. Dunstan, The incorporation of strontium and zinc into a calcium–silicon ceramic for bone tissue engineering. Biomaterials, 2010. 31: 3175-3184.

[3] R. Choudhary, J. Vecstaudza, G. Krishnamurithy, H.R.B. Raghavendran, M.R. Murali, T. Kamarul, S. Swamiappan, and J. Locs, In-vitro bioactivity, biocompatibility and dissolution studies of diopside prepared from biowaste by using sol–gel combustion method. Mater. Sci. Eng. C 2016. 68: 89-100.

[4] E.M.A. Hamzawy, A.M. El-Kady, M.I. El Gohary, A.A. El Saied and H.S. Zayed, In vivo bioactivity evaluation for an inexpensive biocompatible composite based on wollastonite ceramic/soda-lime-silica glass. Biomed. Phys. Eng. Express, 2017. 3(4): 045018.

[5] F. Baino, S. Fiorilli and C. Vitale-Brovarone, Bioactive glass-based materials with hierarchical porosity for medical applications: Review of recent advances. Acta Biomater., 2016. 42: 18-32.

[6] S. Kaya, M. Cresswell and A.R. Boccaccini, Mesoporous silica-based bioactive glasses for antibiotic-free antibacterial applications. Mater. Sci. Eng. C 2018. 83: 99-107.

[7] V. Mouriño, R. Vidotto, J.P. Cattalini and A.R. Boccaccini, Enhancing biological activity of bioactive glass scaffolds by inorganic ion delivery for bone tissue engineering. Curr Opin Biomed Eng, 2019. 10: 23-34.

[8] H.R. Bakhsheshi-Rad, M. Akbari, A.F. Ismail, et al., Coating biodegradable magnesium alloys with electrospun poly-L-lactic acid-åkermanitedoxycycline nanofibers for enhanced biocompatibility, antibacterial activity, and corrosion resistance, Surf. Coat. Technol. 2019. 377: 124898.

[9] M. Diba, O.-M. Goudouri, F. Tapia and A.R. Boccaccini, Magnesium-containing bioactive polycrystalline silicate-based ceramics and glass-ceramics for biomedical applications. Curr. Opin. Solid State Mater. Sci., 2014. 18: 147-167.

[10] H.R. Bakhsheshi-Rad, E. Hamzah, N. Abbasizadeh, A. Najafinezhad and M. Kashefian, Synthesis of novel nanostructured bredigite–amoxicillin scaffolds for bone defect treatment: cytocompatibility and antibacterial activity. J. Sol-Gel Sci. Technol., 2018. 86: 83-93.

[11] H. Mohammadi., M. Hafezi., N. Nezafati., S. Heasarki., A. Nadernezhad., S. M. H. Ghazanfari., and M. Sepantafar., Bioinorganics in bioactive calcium silicate ceramics for bone tissue repair: Bioactivity and biological properties. J Ceram Sci Technol., 2014. 5: 1-12.

[12] A. Pal, S. Maity, S. Chabri, S. Bera, A.R. Chowdhury, M. Das, and A. Sinha, Mechanochemical synthesis of nanocrystalline hydroxyapatite from Mercenaria clam shells and phosphoric acid. Biomed. Phys. Eng. Express, 2017. 3(1): 015010.

[13] J.R. Jones, Reprint of: Review of bioactive glass: From Hench to hybrids. Acta Biomater., 2015. 23: S53-S82.

[14] L. Liu, K. Kuffel, D.K. Scott, G. Constantinescu, H.-J. Chung and J. Rieger, Silicone-based adhesives for long-term skin application: cleaning protocols and their effect on peel strength. Biomed. Phys. Eng. Express, 2017. 4(1): 015004.

[15] Q. Yao, H. Liu, X. Lin, L. Ma, X. Zheng, Y. Liu, P. Huang, S. Yu, W. Zhang, M. Lin, and L. Dai, 3D interpenetrated graphene foam/58S bioactive glass scaffolds for electrical-stimulation-assisted differentiation of rabbit mesenchymal stem cells to enhance bone regeneration. J. Biomed. Nanotechnol, 2019. 15: 602-611.

[16] D. Fernando, N. Attik, N. Pradelle-Plasse, P. Jackson, B. Grosgogeat and P. Colon, Bioactive glass for dentin remineralization: A systematic review. Mater. Sci. Eng. C 2017. 76: 1369-1377.

[17] M. Ramya, M.M. Pillai, R. Selvakumar, B. Raj and K.R. Ravi, Hydroxyapatite particle (HAp) reinforced biodegradable Mg-Zn-Ca metallic glass composite for bio-implant applications. Biomed. Phys. Eng. Express, 2018. 4(2): 025039.

[18] M. Gong, Q. Zhao, L. Dai, Y. Li and T. Jiang, Fabrication and Friction Coefficient of Graphene Oxide Reinforced Hydroxyapatite Composite. J Nanosci Nanotechno, 2018. 18: 1893-1900.

[19] L.B. Romero-Sánchez, S. Borrego-González and A. Díaz-Cuenca, High surface area biopolymeric-ceramic scaffolds for hard tissue engineering. Biomed. Phys. Eng. Express. 2017. 3(3): 035012.

[20] C. Wu, Y. Ramaswamy and H. Zreiqat, Porous diopside ($CaMgSi_2O_6$) scaffold: A promising bioactive material for bone tissue engineering. Acta Biomater., 2010. 6: 2237-2245.

[21] Y. Ramaswamy, C. Wu, H. Zhou and H. Zreiqat, Biological response of human bone cells to zinc-modified Ca–Si-based ceramics. Acta Biomater., 2008. 4(5): 1487-1497.

[22] H.R. Bakhsheshi-Rad, E. Hamzah, A.F. Ismail, M. Aziz, Z. Hadisi, M. Kashefian, and A. Najafinezhad, Novel nanostructured baghdadite-vancomycin scaffolds: In-vitro drug release, antibacterial activity and biocompatibility. Mater. Lett. 2017. 209: 369-372.

[23] F. Pahlevanzadeh, H. R. Bakhsheshi-Rad, et al, Apatite-forming ability, cytocompatibility, and mechanical properties enhancement of poly methyl methacrylate-based bone cements by incorporating of baghdadite nanoparticles, Int J Appl Ceram Technol. 2019; 16: 2006-2019.

[24] M. Meyyappan, L. Jing, L. Jun and A. Cassell. Nanotechnology: An Overview and Integration with MEMS. in 19th IEEE International Conference on Micro Electro Mechanical Systems. 2006.

[25] M. Meyyappan. Novel one dimensional nanostructures. in 2005 International Conference on MEMS,NANO and Smart Systems. 2005.

[26] M. Meyyappan. Nanotechnology: Development of practical systems and nano-micro-macro integration. in 2015 IEEE Regional Symposium on Micro and Nanoelectronics (RSM). 2015.

[27] B. Yu and M. Meyyappan. Nanotechnology: potential challenger to silicon CMOS? in Proceedings of 35th European Solid-State Device Research Conference, 2005. ESSDERC 2005. 2005.

[28] C. Chen, P. Watkins-Curry, M. Smoak, K. Hogan, S. Deese, G.T. McCandless, J.Y. Chan, and D.J. Hayes, Targeting calcium magnesium silicates for polycaprolactone/ceramic composite scaffolds. ACS Biomater. Sci. Eng. 2015. 1: 94-102.

[29] H.R. Bakhsheshi-Rad, E. Hamzah, A.F. Ismail, et al, Synthesis of a novel nanostructured zinc oxide/baghdadite coating on Mg alloy for biomedical application: In-vitro degradation behavior and antibacterial activities. Ceram. Int., 2017. 43(17): 14842-14850.

[30] R.G. Ribas, V.M. Schatkoski, T.L.d.A. Montanheiro, B.R.C. de Menezes, C. Stegemann, D.M.G. Leite, and G.P. Thim, Current advances in bone tissue engineering concerning ceramic and bioglass scaffolds: A review. Ceram. Int. 2019.

[31] G. Kaur, V. Kumar, F. Baino, J.C. Mauro, G. Pickrell, I. Evans, and O. Bretcanu, Mechanical properties of bioactive glasses, ceramics, glass-ceramics and composites: State-of-the-art review and future challenges. Mater. Sci. Eng. C 2019. 104: 109895.

[32] N.Y. Iwata, G.-H. Lee, S. Tsunakawa, Y. Tokuoka and N. Kawashima, Preparation of diopside with apatite-forming ability by sol–gel process using metal alkoxide and metal salts. Colloids Surf. B 2004. 33: 1-6.

[33] C. Wu, J. Chang and W. Zhai, A novel hardystonite bioceramic: preparation and characteristics. Ceram. Int. 2005. 31: 27-31.

[34] G. Wang, Z. Lu, D. Dwarte and H. Zreiqat, Porous scaffolds with tailored reactivity modulate in-vitro osteoblast responses. Mater. Sci. Eng. C 2012. 32: 1818-1826.

[35] K. Xiong, H. Shi, J. Liu, Z. Shen, H. Li and J. Ye, Control of the Dissolution of Ca and Si Ions from CaSiO3 Bioceramic via Tailoring Its Surface Structure and Chemical Composition. J. Am. Ceram. Soc. 2013. 96: 691-696.

[36] H.R. Bakhsheshi-Rad, X.B. Chen, A.F. Ismail, M. Aziz, E. Hamzah and A. Najafinezhad, A new multifunctional monticellite-ciprofloxacin scaffold: Preparation, bioactivity, biocompatibility, and antibacterial properties. Mater. Chem. Phys. 2019. 222: 118-131.

[37] Kokubo T, Takadama H. How useful is SBF in predicting in vivo bone bioactivity? Biomaterials 2006. 27: 2907–15.

[38] M. Eilbagi, R. Emadi, K. Raeissi, M. Kharaziha and A. Valiani, Mechanical and cytotoxicity evaluation of nanostructured hydroxyapatite-bredigite scaffolds for bone regeneration. Mater. Sci. Eng. C 2016. 68: 603-612.

[39] G.K. Williamson. and W.H. Hall., X-ray line broadening from filed aluminium and wolfram. Acta Metall. 1953. 1: 22-31.

[40] A. Farzin, M. Fathi, R. Emadi, Multifunctional magnetic nanostructured hardystonite scaffold for hyperthermia, drug delivery and tissue engineering applications, Mater. Sci. Eng. C 2017. 70: 21-31.

[41] S. Ramezani, R. Emadi, M. Kharaziha and F. Tavangarian, Synthesis, characterization and in vitro behavior of nanostructured diopside/biphasic calcium phosphate scaffolds. Mater. Chem. Phys., 2017. 186: 415-425.

[42] A. Najafinezhad, M. Abdellahi, S. N. Harchegani, A. Soheily, M. Khezri, H. Ghayour, On the synthesis of nanostructured akermanite scaffolds via space holder method: The effect of the spacer size on the porosity and mechanical properties, J. Mech. Behav. Biomed. Mater. 69 (2017) 242–248.

[43] M.H.R. Zadeh, M. Seifi, M. Abdolrahimi and M. Hadavi, A comprehensive in vitro study of the carbon nanotube enhanced chitosan scaffolds for cancellous bone regeneration. Biomedical Biomed. Phys. Eng. Express, 2018. 4(3): 035027.

[44] G. Mestres, R.A. Perez, N.L. D'Elía and L. Barbe, Advantages of microfluidic systems for studying cell-biomaterial interactions—focus on bone regeneration applications. Biomed. Phys. Eng. Express, 2019. 5(3): 032001.

[45]H. Ghomi, R. Emadi and S.H. Javanmard, Fabrication and characterization of nanostructure diopside scaffolds using the space holder method: Effect of different space holders and compaction pressures. Mater. Des. 2016. 91: 193-200.

[46]C. Liu, J. Zhang, J. Sun, X. Zhang and Y. Hu, Addition of Al–Ti–C master alloys and diopside to improve the performance of alumina matrix ceramic materials. Ceram. Int. 2007. 33: 1149-1154.

[47] H.R. Bakhsheshi-Rad, E. Hamzah, A.F. Ismail, M. Aziz, A. Najafinezhad and M. Daroonparvar, Synthesis and in-vitro performance of nanostructured monticellite coating on magnesium alloy for biomedical applications. J. Alloys Compd. 2019. 773: 180-193.

[48] Sadeghzade, S., R. Emadi and S. Labbaf, Hardystonite-diopside nanocomposite scaffolds for bone tissue engineering applications. Mater. Chem. Phys. 2017. 202: 95-103.

[49] H.R. Bakhsheshi-Rad, E. Hamzah, M. Kasiri-Asgarani, S. Jabbarzare, M. Daroonparvar and A. Najafinezhad, Fabrication, degradation behavior and cytotoxicity of nanostructured hardystonite and titania/hardystonite coatings on Mg alloys. Vacuum, 2016. 129: 9-12.

Caption of Figures

Fig. 1. Fabrication procedure of hardystonite-diopside scaffolds

Fig. 2 (a) X-ray diffraction pattern and (b) FTIR absorption spectra of hardystonite-diopside scaffolds with various diopside amounts

Fig. 3 TEM micrograph (a) hardystonite, (b) diopside, and (c) hardystonite-diopside nanopowders and d) EDX spectrum of HT-12.5%Di scaffold

Fig. 4. SEM images of hardystonite (a) and hardystonite-diopside scaffolds with various diopside amount: 5 (b), 12.5 (c), and 25 wt.% (d) and corresponding distribution of pore size

Fig. 5. Compressive stress–strain curve of hardystonite-diopside scaffolds with various diopside amounts

Fig. 6 SEM images of HT (a), HT-5Di (b), HT-12.5Di (c), and HT-25Di (d) scaffolds after 28 d immersion in SBF solution

Fig. 7 EDS mapping of HT (a), HT-5Di (b), HT-12.5Di (c), and HT-25Di (d) scaffolds after 28 d immersion in SBF solution

Fig. 8 Schematic representation of the mechanism of apatite formation on the surface of hardystonite-diopside in the SBF solution

Fig. 9 (a) pH changes in the SBF solution (b) weight loss and (c) FTIR absorption spectra of the hardystonite-diopside scaffolds after soaking in the SBF

Fig. 10 DAPI staining of MG-63 cells cultured on a hardystonite scaffold (a) and hardystonite-diopside scaffolds with 5 (b), 12.5 (c), and 25 wt.% (d) diopside. Viability of MG-63 cells cultured for 3 and 5 days on hardystonite-diopside (e) scaffolds

Fig. 11 Alizarin red staining of MG-63 cells cultured on (a) HT and HT-Di scaffolds containing various diopside content: (b) 5, (c) 12.5, (d) 25 wt.%

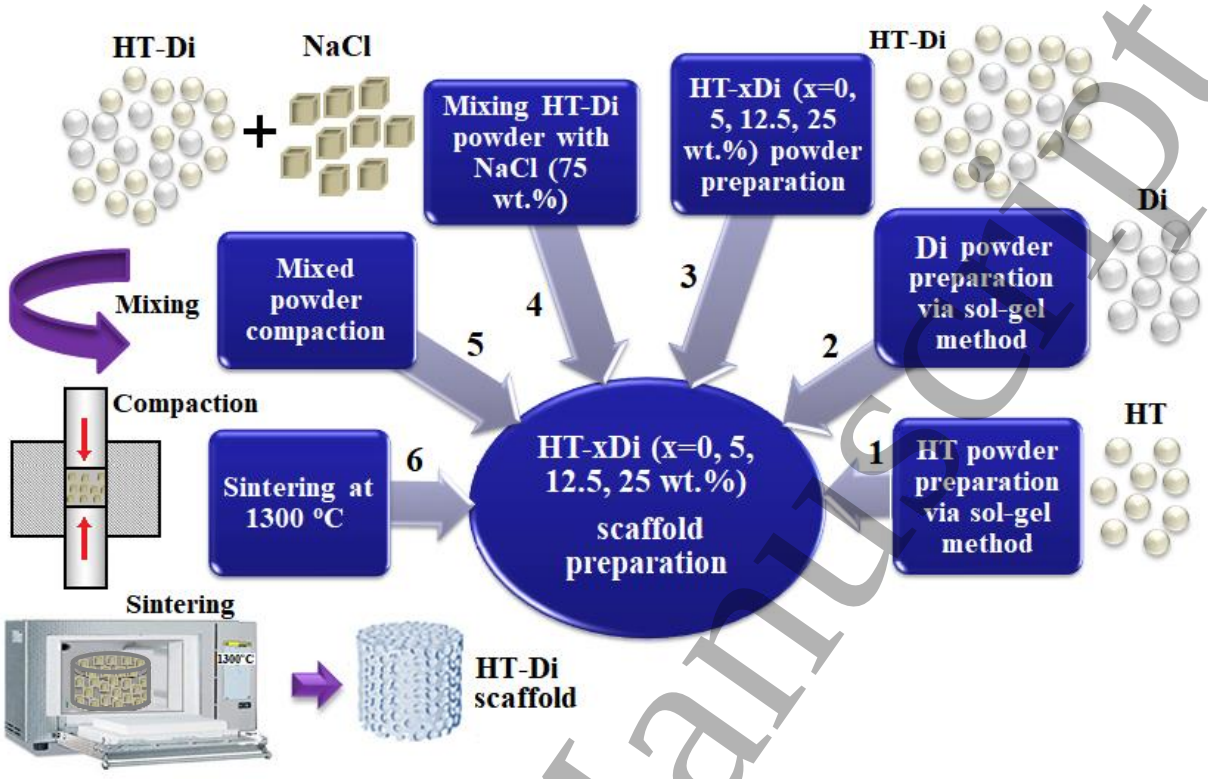

Fig. 1. Fabrication procedure of hardystonite-diopside scaffolds

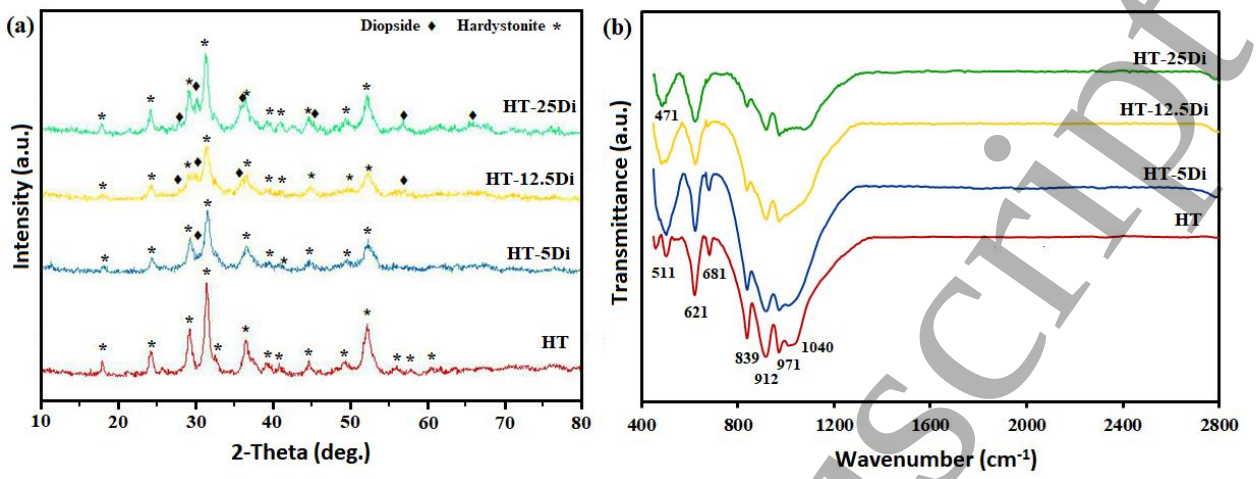

Fig. 2 (a) X-ray diffraction pattern and (b) FTIR absorption spectra of hardystonite-diopside scaffolds with various diopside amounts

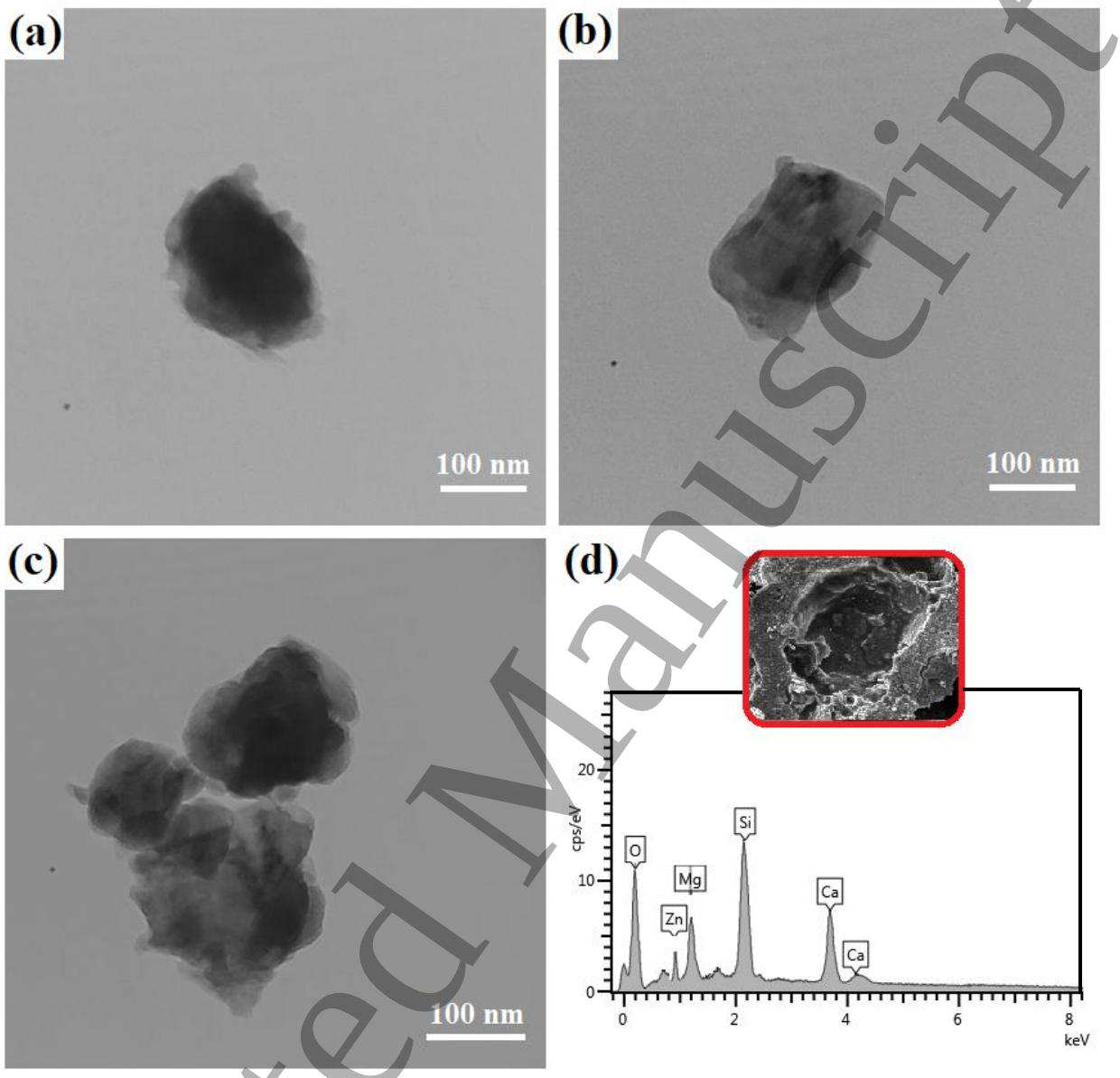

Fig. 3 TEM micrograph (a) hardystonite, (b) diopside, and (c) hardystonite-diopside nanopowders and d) EDX spectrum of HT-12.5%Di scaffold

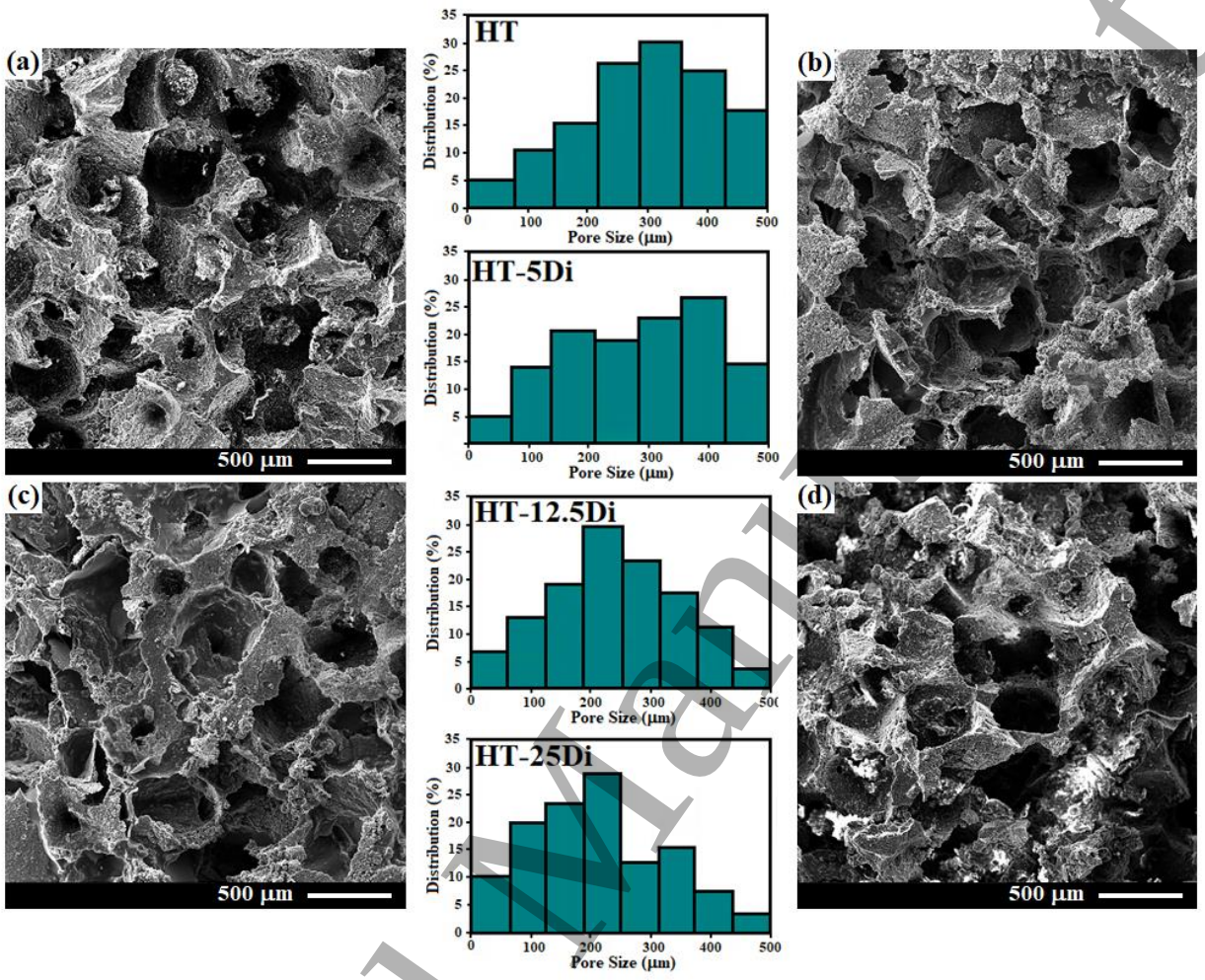

Fig. 4. SEM images of hardystonite (a) and hardystonite-diopside scaffolds with various diopside amount: 5 (b), 12.5 (c), and 25 wt.% (d) and corresponding distribution of pore size

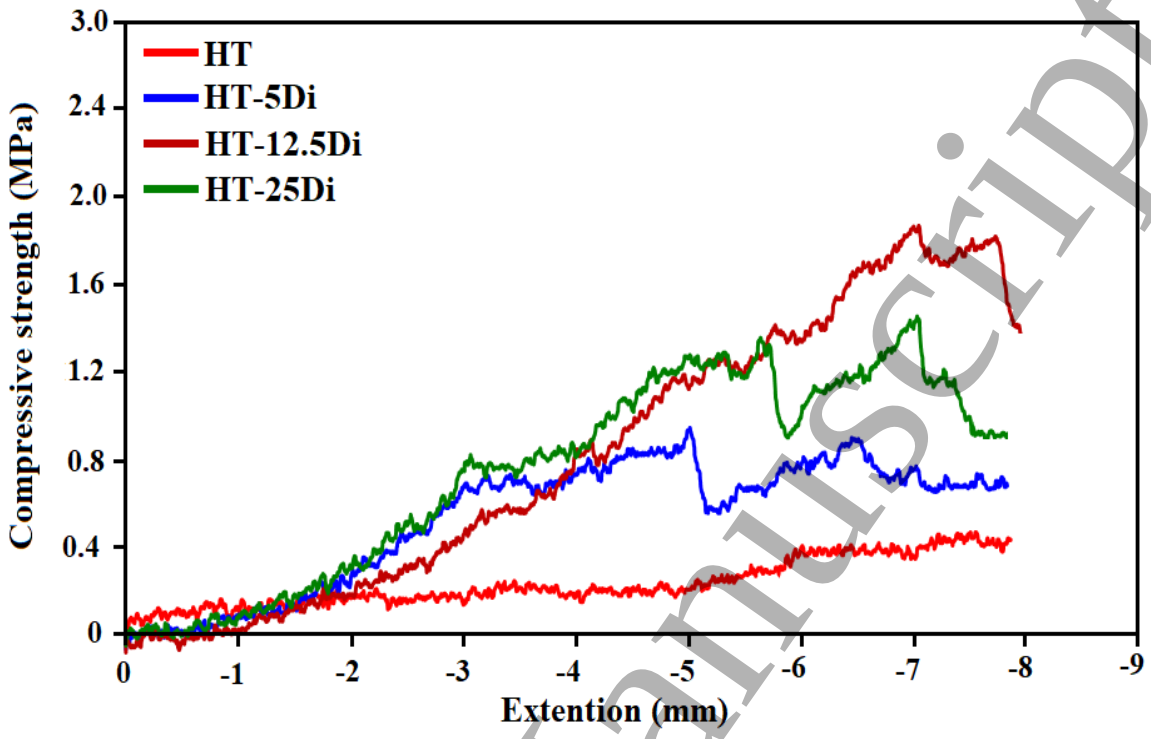

Fig. 5. Compressive stress–strain curve of hardystonite-diopside scaffolds with various diopside amounts

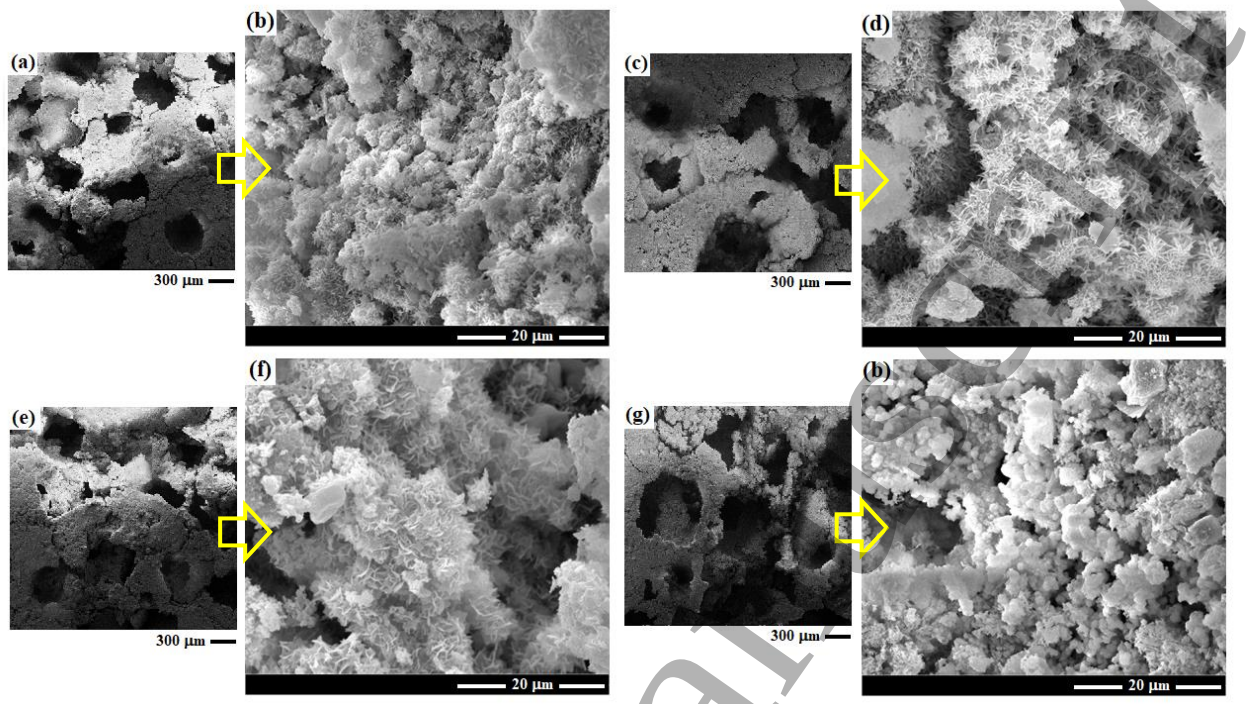

Fig. 6 SEM images of HT (a), HT-5Di (b), HT-12.5Di (c), and HT-25Di (d) scaffolds after 28 d immersion in SBF solution

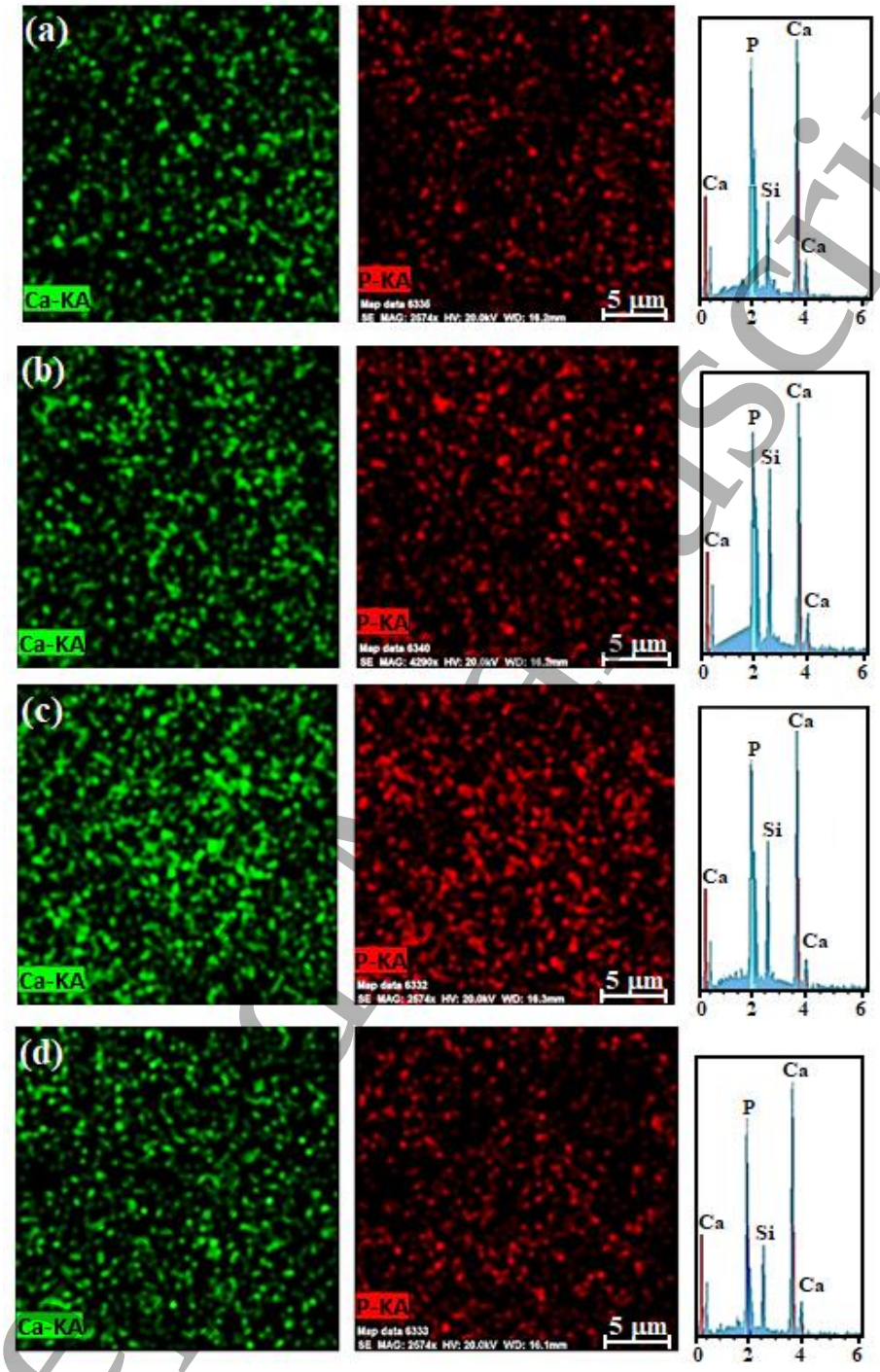

Fig. 7 EDS mapping of HT (a), HT-5Di (b), HT-12.5Di (c), and HT-25Di (d) scaffolds after 28 d immersion in SBF solution

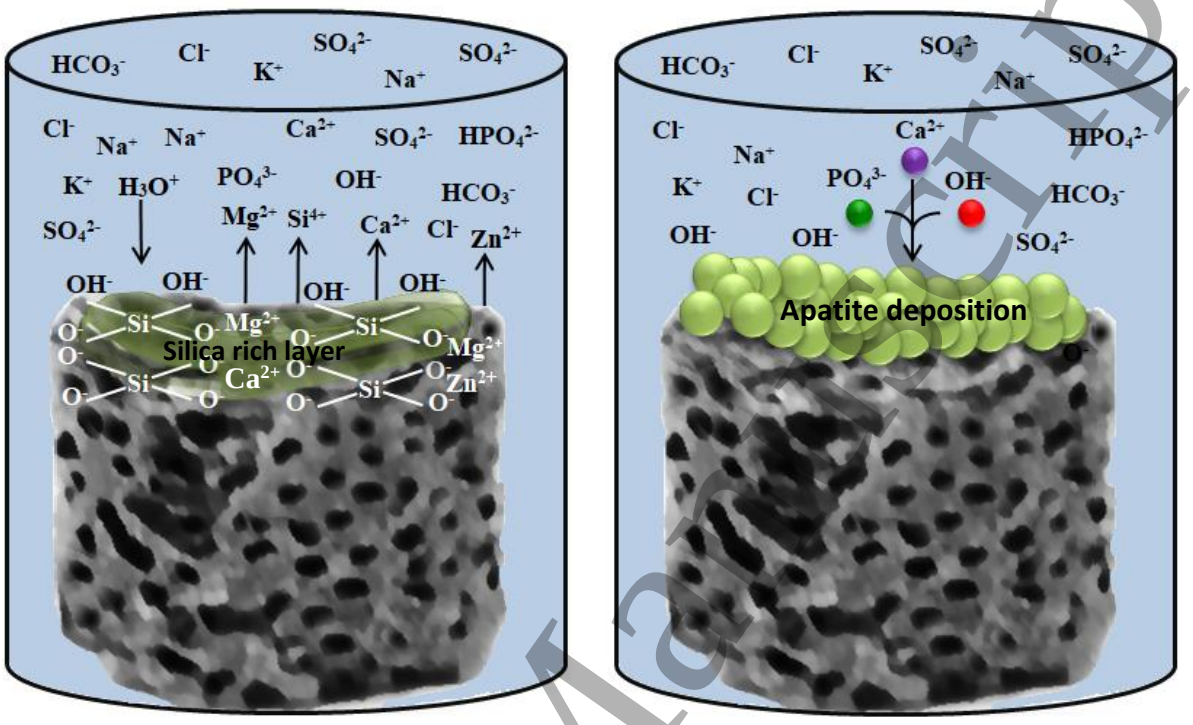

Fig. 8 Schematic representation of the mechanism of apatite formation on the surface of hardystonite-diopside in the SBF solution

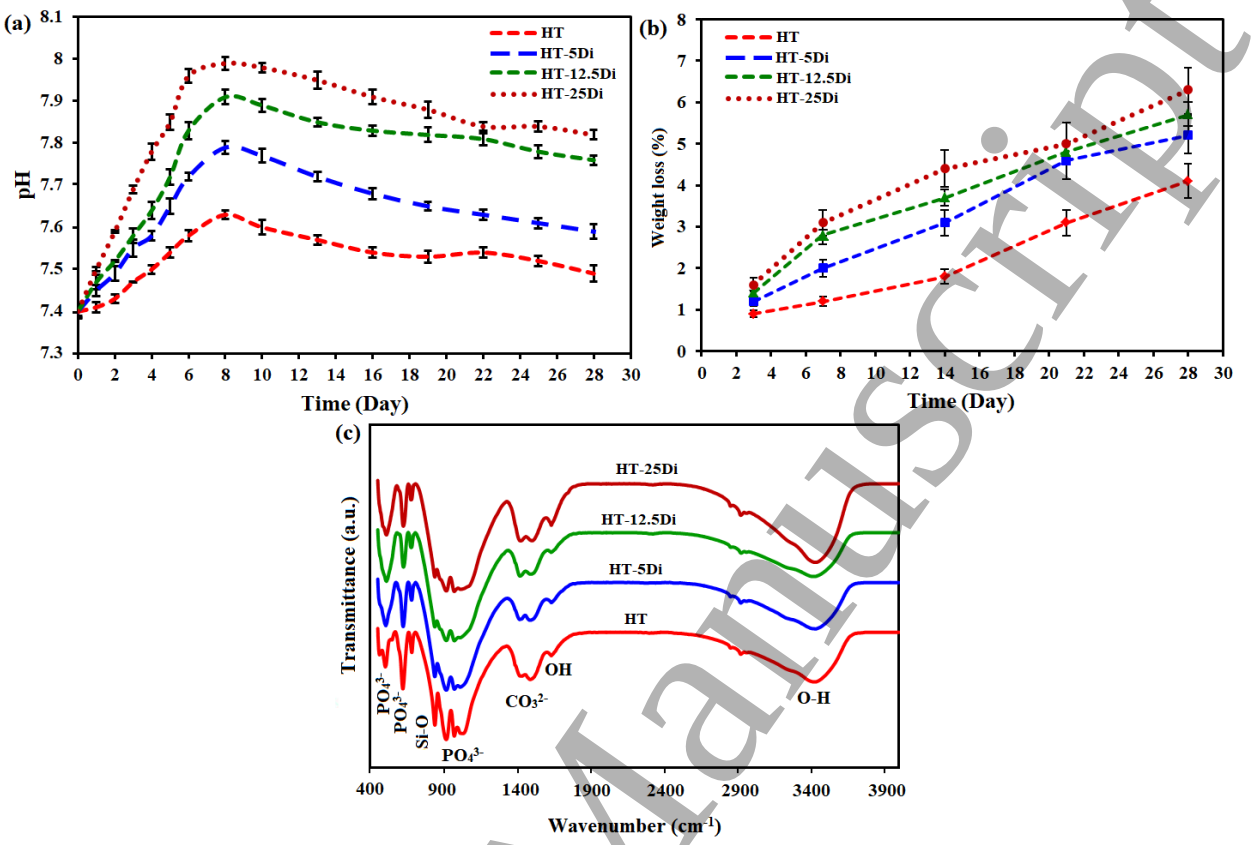

Fig. 9 (a) pH changes in the SBF solution (b) weight loss and (c) FTIR absorption spectra of the hardystonite-diopside scaffolds after soaking in the SBF

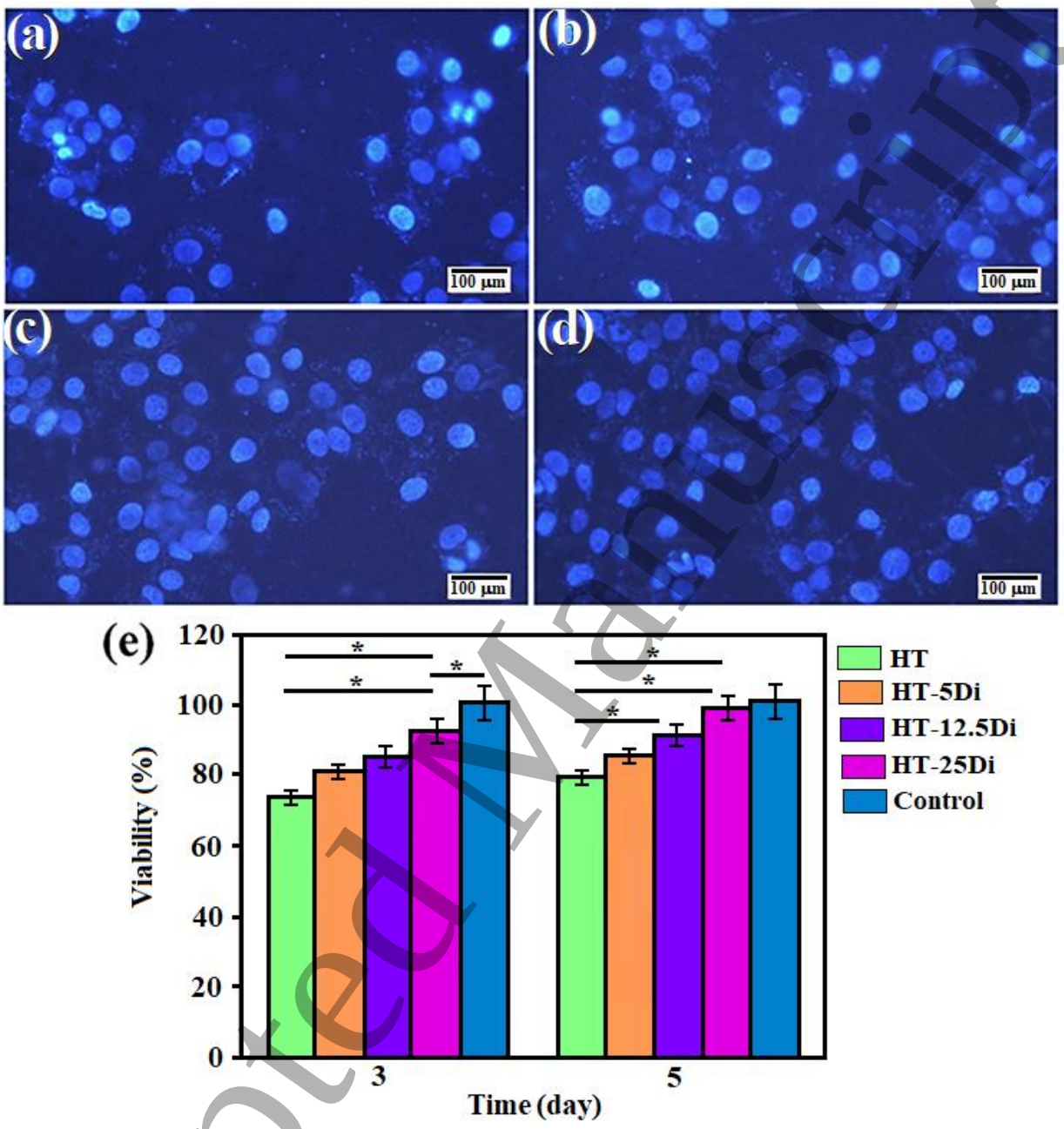

Fig. 10 DAPI staining of MG-63 cells cultured on a hardystonite scaffold (a) and hardystonite-diopside scaffolds with 5 (b), 12.5 (c), and 25 wt.% (d) diopside. Viability of MG-63 cells cultured for 3 and 5 days on hardystonite-diopside (e) scaffolds.

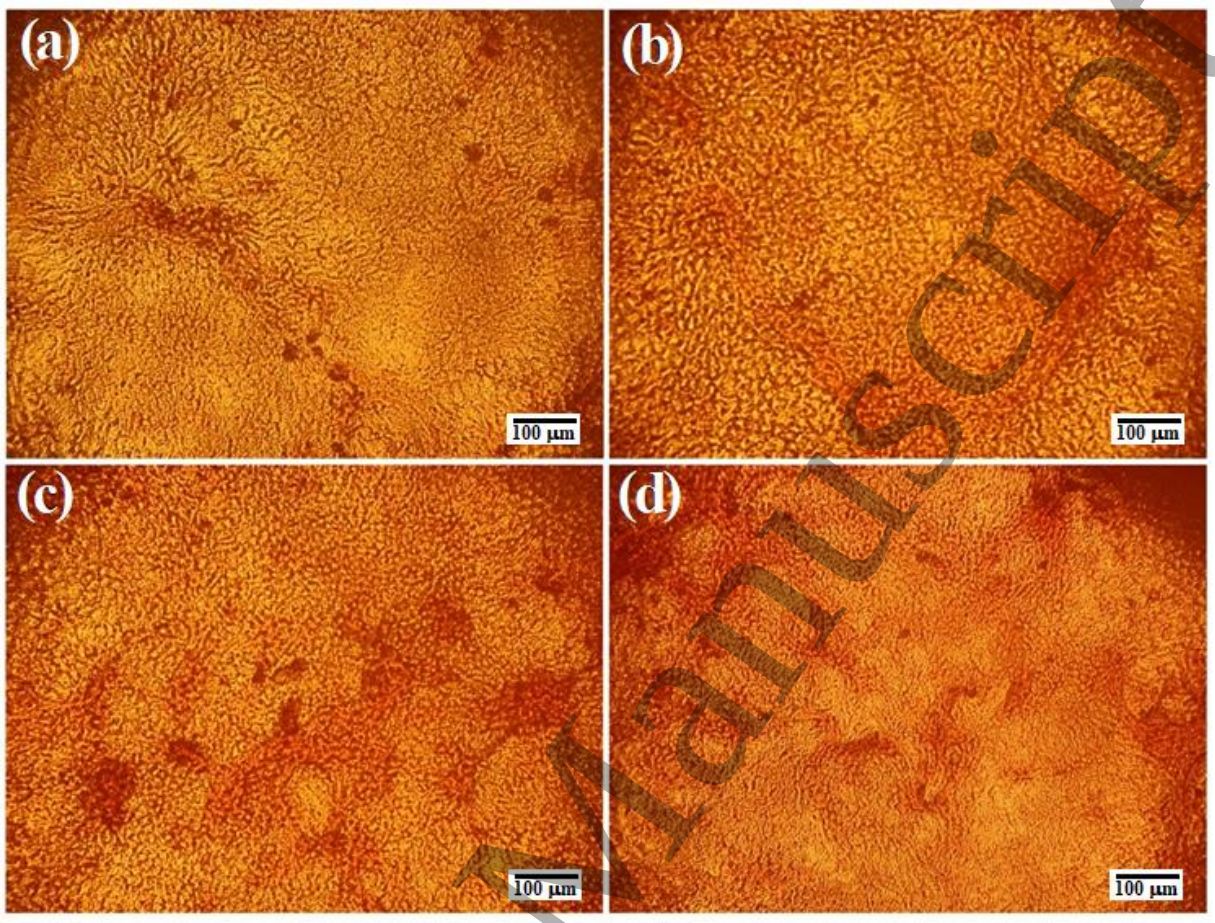

Fig. 11 Alizarin red staining of MG-63 cells cultured on (a) HT and HT-Di scaffolds containing various diopside content: (b) 5, (c) 12.5, (d) 25 wt.%

Table 1 Chemical composition of the Kokubo simulated body fluid (SBF) compared to the human blood plasma

Solution	Ion concentration (mmol/L)							
	Na^+	K^+	Ca^{2+}	Mg^{2+}	HCO_3^-	Cl^-	HPO_4^{2-}	SO_4^{2-}
Plasma	142.0	5.0	2.5	1.5	27.0	103.0	1.0	0.5
Kokubo (c–SBF)	142.0	5.0	2.5	1.5	4.2	147.8	1.0	0.5